AIMS Mathematics, 11(6): 15376–15401.
DOI: 10.3934/math.2026632
Received: 30 March 2026
Revised: 06 May 2026
Accepted: 21 May 2026
Published: 01 June 2026

https://www.aimspress.com/journal/Math

Research article

Analytical solutions, bifurcations, and chaotic patterns of the Sasa-Satsuma equation via the $exp(-\Phi(\zeta))$ expansion method

B. Alreshidi[1], Abdulaziz Almaslokh[1], A.A. Elsadany[1,*] and Mohammed. K. Elboree[2]

[1] Department of Mathematics, Faculty of Sciences and Humanities in Al-Kharj, Prince Sattam bin Abdulaziz University, Al-Kharj 11942, Saudi Arabia

[2] Department of Mathematics, Faculty of Science, Qena University, Qena 83523, Egypt

* **Correspondence:** Email: aelsadany1@yahoo.com.

Abstract: In this study, the propagation of ultrashort optical pulses in nonlinear dispersive media with third-order dispersion, self-steepening, and stimulated Raman scattering is modelled using the Sasa-Satsuma higher-order nonlinear Schrödinger equation. Exact travelling wave solutions, including bright solitons, dark solitons, singular solutions, and periodic wave solutions, are obtained by applying a travelling wave transformation and applying the $\exp(-\Phi(\zeta))$ function method on the resulting ordinary differential equation. A systematic bifurcation analysis of the associated planar Hamiltonian dynamical system validates these solutions, identifying equilibrium points, constructing phase portraits across all parameter regimes, and explicitly linking orbit families to solution types. Chaotic dynamics are analyzed using time series and phase diagrams. Using Poincaré sections, Lyapunov exponent spectra, time series, and bifurcation diagrams, we map the transition from regular to chaotic regimes and demonstrate how sensitivity to initial conditions governs predictability. The sensitivity analysis shows us the point at which the system becomes very sensitive to changes in the parameter values, which measures how uncertainties in initial conditions and parameters propagate and grow over time in the system.

Keywords: Sasa-Satsuma equation; higher-order nonlinear Schrödinger equation; bifurcation analysis; phase portrait; chaotic dynamics; traveling wave solutions; Poincaré section
Mathematics Subject Classification: 35Q51, 35Q53, 37K40

1. Introduction

The nonlinear Schrödinger equation (NLSE) is considered one of the most significant mathematical models in modern physics, as it offers a general framework for the description of the dynamics of slowly varying wave envelopes in nonlinear and dispersive media. The NLSE has applications in a wide

range of physical environments, from nonlinear optical fibers to plasma physics and Bose-Einstein condensates [1–3]. As far as the area of optical communications is considered, the conventional NLSE accurately describes the essential balance between group velocity dispersion and the Kerr effect, which is responsible for the existence of optical solitons [4]. The theoretical possibility of optical soliton propagation in optical fibers was considered by Hasegawa and Tappert [2], and this achievement is considered one of the major milestones in the development of nonlinear photonics.

With the advent of technological advances that have enabled the achievement of optical pulse durations in the femtosecond range, the physical picture described by the standard NLSE is becoming increasingly inadequate. In the ultra-short time scale of femtosecond pulses, several higher-order effects become relevant, influencing the pulse evolution in a measurable fashion. In this regard, third-order dispersion, self-steepening via the intensity dependence of the group velocity, and stimulated Raman scattering via the delayed nonlinear response of the fiber material are the most physically important effects [5]. The failure of the standard NLSE to incorporate these effects has been shown to cause qualitative discrepancies between theory and experiment, leading to the formulation of the higher-order NLSEs that incorporate these effects. An especially significant example of a higher-order equation in this context is the Sasa-Satsuma equation (SSE), which was originally introduced by Sasa and Satsuma [6] as a generalization of the NLSE that simultaneously accounts for third-order dispersion, self-steepening, and stimulated Raman scattering effects. The integrability of this equation, as proved by the IST technique, has led to it being used as a typical example in investigations of ultrashort pulse dynamics [7]. Extensions of this integrability structure were used by Nimmo & Yilmaz [8] to obtain exact multi-soliton solutions using the binary Darboux transformation, as well as by Xu & Fan [9] to examine the initial boundary value problem on the half-line using the unified transform method. The solution space of the SSE is particularly rich, with this equation being able to support rogue wave solutions in chaotic wave fields [10], as well as a wide range of other localized and oscillatory wave forms, as has been demonstrated through recent analytical investigations [11]. Complementing the analytical methods, the qualitative theory of dynamical systems has been found to provide a highly effective geometric framework for describing the solution structure of nonlinear wave equations. Indeed, when a traveling wave hypothesis is used to reduce a given nonlinear wave equation, one is led to study an ordinary differential equation that can be expressed as a planar autonomous dynamical system, with phase portraits describing the entire topology of solution families. Li [12] carefully developed the bifurcation technique, which was then further developed by Chen [13]. This technique has been found to be a complete framework for describing equilibrium points, bifurcations, and the link between phase portraits and physically important wave solutions. In this framework, homoclinic orbits represent solitary wave solutions, periodic orbits signify periodic travelling waves, and heteroclinic orbits denote kink/anti-kink wave solutions [14]. The effectiveness of this method has been validated through its implementation on various nonlinear wave equations, resulting in a thorough categorization of travelling wave solutions [15].

This Figure 1 summarizes the overall methodology adopted in this paper. Each branch is developed independently in the sections that follow and the results are synthesized in the conclusion.

Another fundamental characteristic of nonlinear wave dynamics is the formation of chaotic motions when the system is subject to external perturbations. Even in circumstances when the unperturbed system is integrable or nearly integrable, the addition of a periodic perturbation can induce the loss of regular motion and the commencement of chaotic dynamics. The study of such effects employs

the usual set of numerical techniques, each of which offers insight into different aspects of the chaotic motions. These techniques include time series analysis, two-dimensional phase diagrams, Poincaré maps, Lyapunov spectra, and bifurcation diagrams [16, 17]. These techniques have proven successful in the study of chaos in various NLSE-type systems, highlighting the role of the amplitude and the frequency of the perturbations in controlling the onset of chaotic motions [18–20]. The importance of such chaotic pulse motions in optical fibers is obvious in terms of signal degradation and loss of signal transmission efficiency.

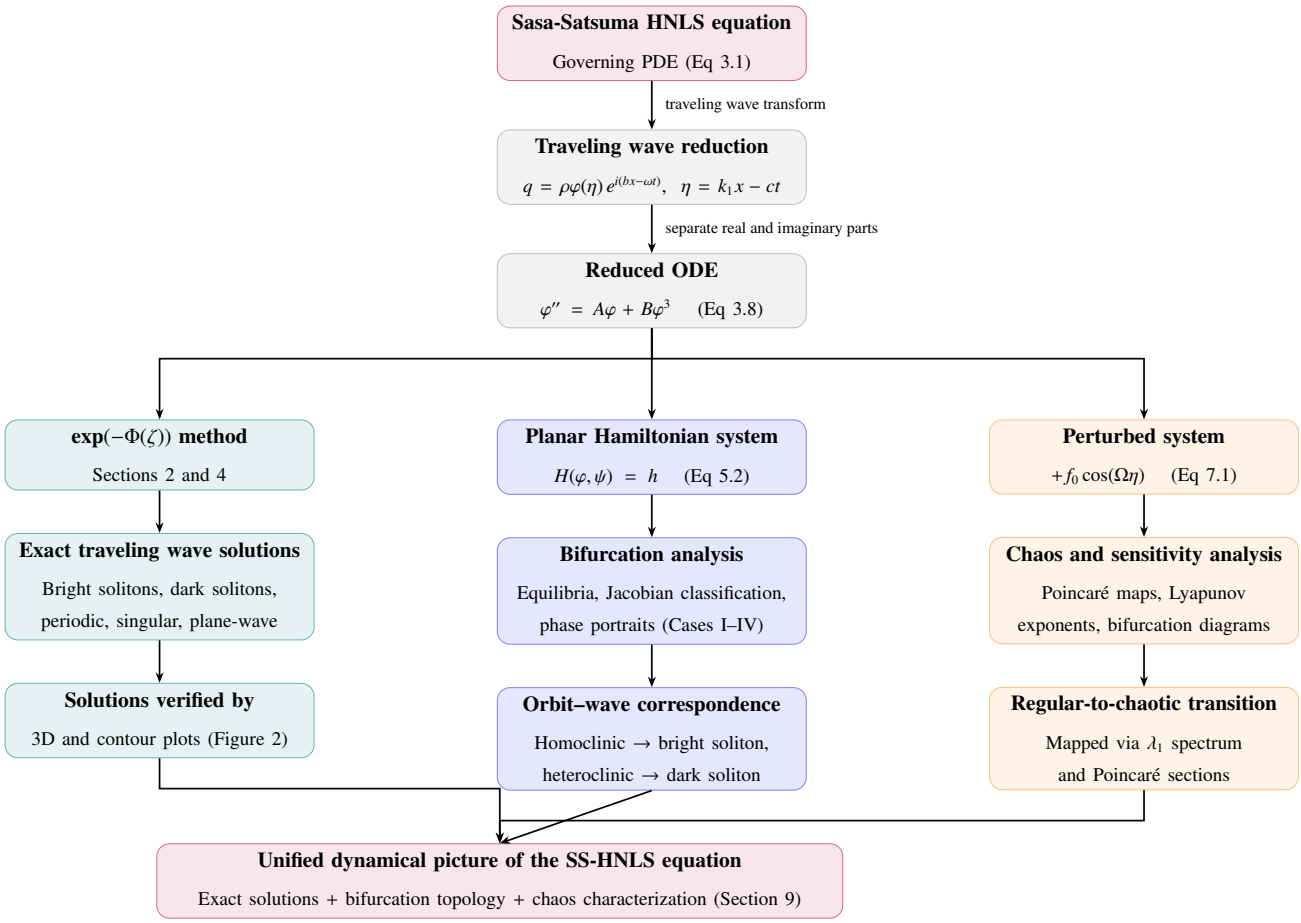

Figure 1. Overall methodology of the paper. The governing SS-HNLS Eq (3.1) is reduced via a traveling wave transformation to the ODE (3.8), which is then analyzed through three complementary branches: **Branch 1** applies the $\exp(-\Phi(\eta))$ expansion method to derive exact closed-form traveling wave solutions; **Branch 2** reformulates the ODE as a planar Hamiltonian system and performs bifurcation and phase portrait analysis; **Branch 3** introduces a periodic perturbation to study chaotic dynamics and sensitivity to initial conditions. All three branches converge to a unified dynamical picture of the SS-HNLS equation (Section 9).

Despite the significant amount of literature published on the issue of integrability and exact solutions of the Sasa-Satsuma equation, a dynamical systems study, including both bifurcation theory and chaotic

theory under periodic perturbation, has not been carried out for this equation. This work fills in this gap by conducting a detailed dynamical systems study of the Sasa-Satsuma higher-order nonlinear Schrödinger equation, using the combined theory of planar dynamical systems and numerical chaos theory. This is done by reducing the equation, using a traveling wave transformation, to a system of equations in the plane, whose equilibrium points are analyzed and whose phase portraits are presented in detail. The onset of chaotic behavior under an external periodic perturbation is then analyzed using various numerical tools.

The rest of this paper is organized as follows: in Section 2, we apply the $exp(-\Phi(\eta))$ expansion method to the SS-HNLS equation. In Section 3, we describe the governing equation and reduce it to a planar dynamical system using the traveling wave transformation. In Section 4, we conduct the bifurcation analysis, classify the equilibria, and draw the phase portraits. In Section 5, we examine the chaotic characteristics of the perturbed dynamical system numerically. In Section 6, we draw the conclusions and propose future work.

2. The $exp(-\Phi(\zeta))$ expansion method

Given a set of nonlinear partial differential equations (NLEEs),

$$F(q, q_t, q_x, q_{xt}, q_{xx}, ...) = 0, \tag{2.1}$$

where F is a polynomial in an unknown function $q(x, t)$ and its derivatives.

The steps for this method are as follows:

Step 1. As a way to solve (2.1), we can use traveling wave solutions.

$$q(x, t) = U(\zeta), \zeta = k_1 x - ct, \tag{2.2}$$

where k_1 is the number of waves and c is the speed of the waves. By substituting (2.2) into (2.1), we can turn Eq (2.1) into an ordinary differential equation (ODE) for $U(\eta)$.

$$F(U, -cU', U'', U''', ...) = 0, \tag{2.3}$$

where $'$ is the derivative with respect to η.

Then, the analytical solutions for Eq (2.3) using the $exp(-\Phi(\eta))$ expansion method can be written as

$$U(\zeta) = \Sigma_{i=0}^{N} a_i \exp(-\Phi(\zeta))^i, \tag{2.4}$$

where $a_i \neq 0$ are real constants that will be found later, and $\Phi(\eta)$ satisfies the following ODE

$$\Phi'(\zeta) = \exp(-\Phi(\zeta)) + \alpha \exp(\Phi(\zeta)) + \sigma, \tag{2.5}$$

where α and σ are constants.

The following solutions exist for Eq (2.1):

Case 1: If $\alpha \neq 0$ and $\sigma^2 - 4\alpha > 0$, then

$$\Phi(\zeta) = \ln\left(-\frac{\sqrt{\sigma^2 - 4\,\alpha}\tanh\left(\frac{\sqrt{\sigma^2-4\,\alpha}}{2}(c_1 + \zeta)\right) + \sigma}{2\alpha}\right). \tag{2.6}$$

Case 2: If $\alpha \neq 0$ and $\sigma^2 - 4\alpha < 0$, then

$$\Phi(\zeta) = \ln\left(\frac{\sqrt{4\,\alpha - \sigma^2}\tan\left(\frac{\sqrt{4\alpha-\sigma^2}}{2}(c_1 + \zeta)\right) - \sigma}{2\alpha}\right). \tag{2.7}$$

Case 3: If $\alpha = 0, \sigma \neq 0$, and $\sigma^2 - 4\alpha > 0$, then

$$\Phi(\zeta) = -\ln\left(\frac{\sigma}{\cosh(\sigma(c_1 + \zeta)) + \sinh(\sigma(c_1 + \zeta)) - 1}\right). \tag{2.8}$$

Case 4: If $\alpha \neq 0, \sigma \neq 0$, and $\sigma^2 - 4\alpha = 0$, then

$$\Phi(\zeta) = \ln\left(-\frac{2(\sigma\,(\zeta + c_1) + 2)}{\sigma^2\,(c_1 + \zeta)}\right). \tag{2.9}$$

Case 5: If $\alpha = 0, \sigma = 0$, and $\sigma^2 - 4\alpha = 0$, then

$$\Phi(\zeta) = \ln(\zeta + c_1), \tag{2.10}$$

where c_1 is a constant of integration.

3. Mathematical formulation and traveling wave reduction

3.1. The governing equation

In this paper, we study the Sasa-Satsuma higher-order nonlinear Schrödinger equation (SS-HNLS), describing the propagation of ultrashort optical pulses in a single-mode nonlinear dispersive optical fiber [21]. The equation under consideration is of the form [22]

$$iq_t + \delta_1 q_{xx} + \delta_2|q|^2 q + i\left(\beta_1 q_{xxx} + \beta_2|q|^2 q_x + \beta_3 q\left(|q|^2\right)_x\right) = 0, \tag{3.1}$$

where $q = q(x, t)$ is the complex envelope of the optical field, x denotes the spatial propagation variable, and t is the temporal variable. The real parameters $\delta_1, \delta_2, \beta_1, \beta_2$, and β_3 represent, the group velocity dispersion coefficient, the Kerr nonlinearity coefficient, and the coefficient of perturbation taking into account simultaneously the effects of third-order dispersion, self-steepening, and stimulated Raman scattering, respectively. When $\beta_i = 0, i = (1, 2, 3)$, Eq (3.1) reduces to the standard NLSE.

The Sasa-Satsuma higher-order nonlinear Schrödinger equation (SSE) is a physically motivated model that governs the propagation of ultrashort optical pulses in the femtosecond regime through single-mode optical fibers, extending the classical NLS equation by incorporating three physically essential higher-order effects: third-order dispersion (TOD), which distorts the pulse envelope through the cubic frequency dependence of the fiber wave number; self-steepening (SS), which arises from the intensity dependence of the group velocity and causes progressive asymmetric compression of the pulse trailing edge; and the stimulated Raman scattering-induced soliton self-frequency shift (SSFS), which continuously transfers pulse energy toward longer wavelengths through intrapulse Raman amplification [4–6]. The SSE holds a unique status within the broader hierarchy of higher-order NLS models as its only integrable member in the Painlevé sense that simultaneously encodes all three of these corrections, thereby admitting a Lax pair, infinitely many conservation laws, and exact multi-soliton solutions, whose stability under perturbations makes them highly suitable as carrier pulses in ultrafast optical communication and photonic systems [22, 23].

3.2. Traveling wave transformation

To reduce Eq (3.1) to a planar dynamical system, we introduce the traveling wave transformation

$$q(x,t) = \rho\varphi(k_1 x - ct)\,\mathrm{e}^{\mathrm{i}(bx-\omega t)}, \qquad \eta = k_1 x - ct, \tag{3.2}$$

where $\varphi(\eta) \geq 0$ is the real-valued wave amplitude, and c is the wave propagation speed.

The parameter b is the carrier wave number, k_1 denotes the wave number, and ω represents the angular frequency. Substituting (3.2) into Eq (3.1) and separating real and imaginary parts, we obtain two coupled ordinary differential equations.

Real part:

$$\left(b\beta_1 - \frac{\delta_1}{3}\right)k_1^2\varphi_{\eta\eta} - \frac{\left(b^3\beta_1 - (b\beta_2 - \delta_2)\,\rho^2\varphi^2 - b^2\delta_1 + \omega\right)\varphi}{3} = 0. \tag{3.3}$$

Imaginary part:

$$\left(-\frac{(\beta_2 + 2\beta_3)\,\rho^2 k_1\varphi^2}{3} + \left(b\beta_1 - \frac{2\delta_1}{3}\right)bk_1 + \frac{c}{3}\right)\varphi_\eta - \frac{\varphi_{\eta\eta\eta}\beta_1 k_1^3}{3} = 0. \tag{3.4}$$

3.3. Reduction to a planar dynamical system

To decouple the system, we impose the constraint arising from the real part Eq (3.3). Integrating once with respect to η and setting the integration constant to zero, corresponding to localized solutions that vanish at infinity, we obtain the following consistency condition on the wave speed ω, β_1, and δ_2

$$\omega = -b^3\beta_1 + b^2\delta_1, \qquad \beta_1 = \frac{\delta_1}{3b}, \qquad \delta_2 = b\beta_2. \tag{3.5}$$

This dispersion relation determines ω entirely in terms of the physical parameters b, δ_1, and β_1. Under condition (3.5), Eq (3.3) is automatically satisfied, and the imaginary part Eq (3.4) reduces to a single second-order ordinary differential equation (ODE) for $\phi(\eta)$:

$$\varphi_{\eta\eta} = \frac{\left(b^3\beta_1 - (b\beta_2 - \delta_2)\,\rho^2\varphi^2 - b^2\delta_1 + \omega\right)\varphi}{3\left(b\beta_1 - \frac{\delta_1}{3}\right)k_1^2}. \tag{3.6}$$

For notational convenience, we introduce the composite parameters

$$A = -\frac{(3bk_1\delta_1 - 3c)\,b}{\delta_1 k_1^3}, \qquad B = -\frac{\rho^2\,(\beta_2 + 2\beta_3)\,b}{k_1^2\delta_1}, \tag{3.7}$$

so that Eq (3.6) takes the compact form

$$\varphi'' = A\varphi + B\varphi^3. \tag{3.8}$$

4. Application of the $exp(-\Phi(\eta))$ expansion method to SS-HNLS equation

Balancing φ^3 and $\varphi_{\eta\eta}$ in Eq (3.8) gives $N = 1$, then Eq (2.4) becomes

$$\varphi(\eta) = a_0 + a_1 \exp(-\Phi(\eta)). \tag{4.1}$$

Substituting Eq (4.1) into Eq (3.8) using Eq (2.5) and collecting all terms of the same power of $exp(-\Phi(\eta))$, we obtain the systems of the parameters $A, B, \alpha, \sigma, a_0$, and a_1. Solving it, we can get

$$a_0 = \frac{2\sigma}{3\sqrt{B}}, \qquad a_1 = \pm\frac{1}{\sqrt{B}}, \tag{4.2}$$

where A_2 and B are arbitrary constants.

From Eqs (4.1) and (4.2), we get the family of complex wave solutions according to the formulas Eqs (2.6)–(2.10) as follows:

If $\alpha \neq 0$ and $\sigma^2 - 4\alpha > 0$, the complex dark soliton solutions for Eq (3.1) can be obtained as follows:

$$q(x,t) = \frac{2\left(\sqrt{\sigma^2-4\alpha}\,\tanh\left(\frac{\sqrt{\sigma^2-4\alpha}\,(-ct+k_1x+c_1)}{2}\right)\sigma + \sigma^2 - 3\alpha\right)e^{i(bx-\omega t)}}{\sqrt{B}\left(3\tanh\left(\frac{\sqrt{\sigma^2-4\alpha}\,(-ct+k_1x+c_1)}{2}\right)\sqrt{\sigma^2-4\alpha} + 3\sigma\right)}. \tag{4.3}$$

If $\beta \neq 0$ and $\delta^2 - 4\beta < 0$, the complex periodic solutions for Eq (3.1) can be obtained as follows:

$$q(x,t) = \frac{2\left(\sqrt{-\sigma^2+4\alpha}\,\tan\left(\frac{\sqrt{-\sigma^2+4\alpha}\,(-ct+k_1x+c_1)}{2}\right)\sigma - \sigma^2 + 3\alpha\right)e^{i(bx-\omega t)}}{\sqrt{B}\left(3\tan\left(\frac{\sqrt{-\sigma^2+4\alpha}\,(-ct+k_1x+c_1)}{2}\right)\sqrt{-\sigma^2+4\alpha} - 3\sigma\right)}. \tag{4.4}$$

If $\alpha = 0, \sigma \neq 0$, and $\sigma^2 - 4\alpha > 0$, the complex bright soliton solutions for Eq (3.1) can be obtained as follows:

$$q(x,t) = \frac{\sigma\left(2\,e^{\sigma(-ct+k_1x+c_1)} + 1\right)e^{i(bx-\omega t)}}{\sqrt{B}\,\left(3\,e^{\sigma(-ct+k_1x+c_1)} - 3\right)}. \tag{4.5}$$

If $\alpha \neq 0, \sigma \neq 0$, and $\sigma^2 - 4\alpha = 0$, the complex plane-waves solutions for Eq (3.1) can be obtained in the following form:

$$q(x,t) = \frac{\sigma\left(-8 + (ct - k_1x - c_1)\,\sigma\right)e^{i(bx-\omega t)}}{\sqrt{B}\,\left(-12 + (6ct - 6k_1x - 6c_1)\,\sigma\right)}. \tag{4.6}$$

If $\alpha = 0, \sigma = 0$, the complex plane-waves solutions for Eq (3.1) can be obtained in the following form:

$$q(x,t) = \frac{-3e^{\mathrm{I}(bx-\omega t)}}{\sqrt{B}\,(3ct - 3k_1x - 3c_1)}. \tag{4.7}$$

Figure 2(a) shows the absolute dark-singular optical soliton solutions (4.3) for (3.1) with suitable choice for parameters, Figure 2(b) shows the absolute periodic solutions (4.4) for (3.1) with suitable choice for parameters, and Figure 2(c)–(e) shows the absolute plane-waves optical solutions (4.5)–(4.7)

for (3.1) with suitable choice for parameters. The authors in [24] applied the modified exp-function approaches to complex biological nonlinear systems, while the authors in [25] applied the exp-function methods to higher-order dispersive equations and found the alternative solution method for NLSE-type equations; a comparison with exp-function results can be found in [26].

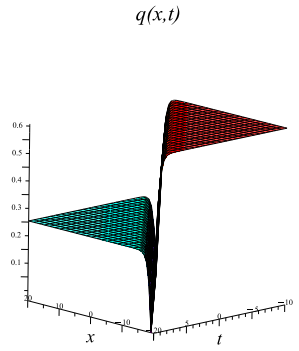

(a) dark solutions when $\alpha \neq 0$ and $\sigma^2 - 4\alpha > 0$

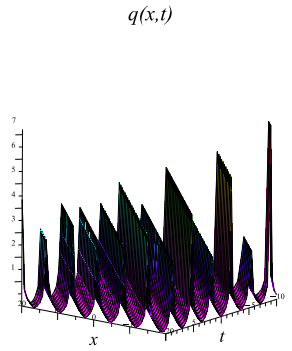

(b) periodic solutions when $\alpha \neq 0$ and $\sigma^2 - 4\alpha < 0$

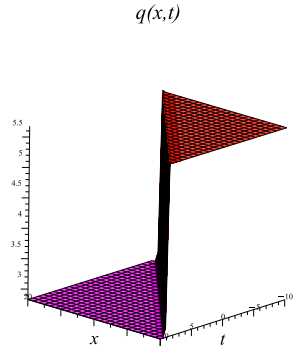

(c) plane-waves solutions when $\alpha = 0, \sigma \neq 0$, and $\sigma^2 - 4\alpha > 0$

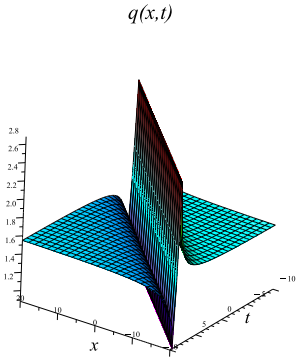

(d) plane-waves solutions when $\alpha \neq 0, \sigma \neq 0$, and $\sigma^2 - 4\alpha = 0$

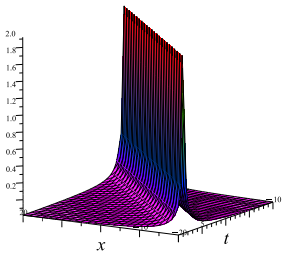

(e) plane-waves solutions when $\alpha = 0, \sigma = 0$, and $\sigma^2 - 4\alpha = 0$

Figure 2. Optical soliton solutions (a)–(e) for (3.1).

5. Bifurcation analysis and chaotic dynamics of the Sasa-Satsuma higher-order nonlinear Schrödinger equation

By setting $\psi = \varphi'$, Eq (3.8) is rewritten as the equivalent planar autonomous dynamical system

$$\begin{cases} \dfrac{d\varphi}{d\eta} = \psi, \\ \dfrac{d\psi}{d\eta} = A\,\varphi + B\,\varphi^3. \end{cases} \tag{5.1}$$

System (5.1) is a Hamiltonian system whose conserved first integral is given by

$$H(\varphi,\, \psi) = \frac{1}{2}\psi^2 - \frac{A}{2}\varphi^2 - \frac{B}{4}\varphi^4 = h. \tag{5.2}$$

The level curves $H(\varphi, \psi) = h$ in the (φ, ψ) phase plane correspond directly to distinct families of traveling wave solutions of the original SS-HNLS Eq (3.1): Homoclinic orbits correspond to solitary wave solutions, closed periodic orbits enclosing a center yield periodic traveling waves, and heteroclinic orbits connecting saddle points give rise to kink-type solutions. A complete classification of these orbit families and the bifurcation conditions under which they arise for the system (5.1) is presented.

In this section, we perform a systematic bifurcation analysis of the planar dynamical system (5.1) obtained from the SS-HNLS equation through the traveling wave reduction (3.2).

5.1. Equilibrium points and linear stability

The equilibrium points of system (5.1) are found by simultaneously setting $d\varphi/d\eta = 0$ and $d\psi/d\eta = 0$, which yields the conditions

$$\psi = 0, \qquad \varphi\left(A + B\,\varphi^2\right) = 0. \tag{5.3}$$

From (5.3), three families of equilibrium points are identified:

- Origin: $E_0 = (0,\, 0)$, which exists for all parameter values.
- Non-trivial equilibria: $E_{\pm} = (\pm\varphi^*,\, 0)$, where $\varphi^* = \sqrt{-A/B}$, which exist if and only if $AB < 0$.

To classify these equilibrium points, we compute the Jacobian matrix of system (5.1) at a general point $(\varphi_0,\, 0)$:

$$\mathbf{J}(\varphi_0) = \begin{pmatrix} 0 & 1 \\ A + 3B\,\varphi_0^2 & 0 \end{pmatrix}. \tag{5.4}$$

The characteristic equation associated with $\mathbf{J}$ is

$$\lambda^2 - \Delta(\varphi_0) = 0, \tag{5.5}$$

where the determinant is $\Delta(\varphi_0) = -(A + 3B\,\varphi_0^2)$, and the trace $\tau = \mathrm{tr}(\mathbf{J}) = 0$ vanishes identically for all parameter values, as expected for a Hamiltonian system. The eigenvalues are

$$\lambda_{1,2} = \pm\sqrt{\Delta(\varphi_0)}, \tag{5.6}$$

from which the stability type of each equilibrium follows directly.

Classification at $E_0 = (0, 0)$:

At the origin, $\Delta(0) = -A$. Therefore,

- If $A > 0$: $\Delta(0) > 0$ and $\lambda_{1,2} = \pm i\sqrt{|A|}$ are purely imaginary, so E_0 is a center.
- If $A < 0$: $\Delta(0) < 0$ and $\lambda_{1,2} = \pm\sqrt{-A}$ are real with opposite signs, so E_0 is a saddle point.
- If $A = 0$: the linearization degenerates, and a separate nonlinear analysis is required; E_0 is a cusp point.

Classification at $E_\pm = (\pm\varphi^*, 0)$:

At the non-trivial equilibria, substituting $\varphi_0^2 = -A/B$ into Δ gives

$$\Delta(\pm\varphi^*) = -\left(A + 3B \cdot \frac{-A}{B}\right) = -(A - 3B) = 2A. \tag{5.7}$$

Hence:

- If $A < 0$ (so that $B > 0$ for $E_\pm$ to exist): $\Delta(E_\pm) = 2A > 0$ and $\lambda_{1,2} = \pm i\sqrt{2A}$, so $E_\pm$ are centers.
- If $A > 0$ (so that $B < 0$ for $E_\pm$ to exist): $\Delta(E_\pm) = 2A < 0$ and $\lambda_{1,2} = \pm\sqrt{2|A|}$, so $E_\pm$ are saddle points.

The classification results are collected in Table 1.

Table 1. Classification of equilibrium points of system (5.1) according to the signs of the parameters A and B.

Case	A	B	$E_0 = (0, 0)$	$E_\pm = (\pm\varphi^*, 0)$	Orbit types
I	> 0	> 0	Center	Do not exist	Unbounded orbits
II	> 0	< 0	Center	Two centers	Periodic + homoclinic orbits
III	< 0	> 0	Saddle	Two saddles	Periodic + heteroclinic orbits
IV	< 0	< 0	Saddle	Do not exist	Unbounded orbits only
V	0	$\neq 0$	Cusp	Do not exist	Degenerate orbits

5.2. Bifurcation conditions

The topological structure of the phase portraits of system (5.1) changes qualitatively when the following bifurcation conditions are met:

Proposition 1. *System* (5.1) *undergoes a pitchfork bifurcation at $A = 0$ when $B \neq 0$. For $AB < 0$, two additional equilibria $E_\pm$ bifurcate from the origin, resulting in a transition between Cases I–IV and Cases II-III in Table 1.*

The Hamiltonian values at the equilibria are very important for figuring out what kinds of orbits there are in the phase plane. Evaluating (6.1) at each equilibrium point, we obtain:

$$H(E_0) = H(0, 0) = 0, \tag{5.8}$$

$$H(E_\pm) = H(\pm\varphi^*, 0) = -\frac{A}{2} \cdot \frac{-A}{B} - \frac{B}{4} \cdot \frac{A^2}{B^2} = \frac{A^2}{4B}. \tag{5.9}$$

The level curve $H(\varphi, \psi) = H(E_{\text{saddle}})$ delineates the separatrix of the system, which segregates topologically distinct families of orbits. Inside the separatrix, orbits are bounded (periodic or homoclinic), whereas those external may be unbounded.

5.3. Phase portrait analysis

We now present the complete phase portrait analysis for each parameter regime. The phase portraits are constructed from the level curves of the Hamiltonian (6.1) and are displayed in Figures 3 and 4.

Case I: $A > 0, B > 0$

The origin E_0 is the only equilibrium point and is a center. The potential function $V(\varphi) = -A\varphi^2/2 - B\varphi^4/4$ is strictly concave at the origin and has no local minima, so no bounded orbits exist. This case supports periodic traveling waves only.

Case II: $A > 0, B < 0$

The origin E_0 is a center with $H(E_0) = 0$, and the two non-trivial equilibria $E_\pm = (\pm\sqrt{A/|B|}, 0)$ are saddles with $H(E_\pm) = A^2/(4B) < 0$. The separatrix passes through the saddle point $E_0 = (0, 0)$ and forms two homoclinic orbits connecting E_0 to itself. Inside each homoclinic loop, a family of periodic orbits encloses the respective center. Trajectories outside the separatrix are unbounded. The homoclinic orbits correspond to bright solitary wave solutions of the original SS-HNLS equation, while the enclosed periodic orbits correspond to periodic traveling wave solutions.

Case III: $A < 0, B > 0$

The origin E_0 is a saddle with $H(E_0) = 0$, and the two non-trivial equilibria $E_\pm = (\pm\sqrt{|A|/B}, 0)$ are centers with $H(E_\pm) = A^2/(4B) > 0$. A family of periodic orbits surrounds the center E_0 for $0 < h < A^2/(4B)$. At the critical level $h = A^2/(4B)$, the separatrix connecting E_+ and E_- forms a pair of symmetric heteroclinic orbits. For $h > A^2/(4B)$, the trajectories are unbounded. The heteroclinic orbits correspond to dark solitary wave solutions, while the innermost periodic orbits correspond to periodic wave solutions of the SS-HNLS equation.

Case IV: $A < 0, B < 0$

The origin E_0 is the only equilibrium point and is a saddle. The potential function achieves a local maximum at the origin, and all orbits sufficiently close to E_0 are periodic. For $h > 0$, the trajectories escape to infinity. This case supports only periodic traveling wave solutions.



(a) Case I: $A > 0,\ B > 0$ (center at E_0)

(b) Case II: $A < 0,\ B < 0$ (center at E_0)

Figure 3. Phase portraits of system when (a) E_0 is a center; (b) E_0 is also a center with homoclinic orbits corresponding to bright soliton solutions.

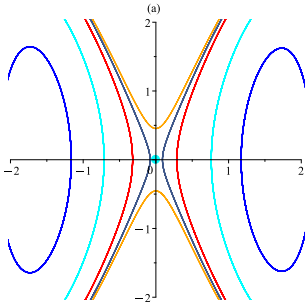

(a) Phase portraits of system when $A > 0$ and $B < 0$

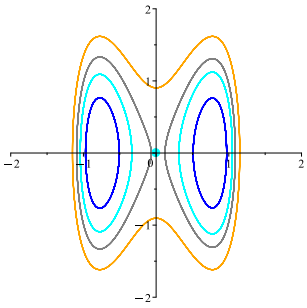

(b) Phase portraits of system when $A > 0$ and $B < 0$

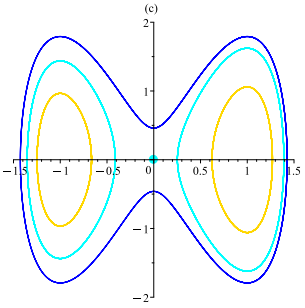

(c) Phase portraits of system when $A > 0$ and $B < 0$

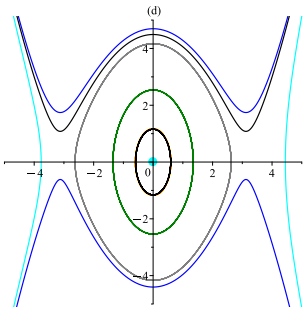

(d) Phase portraits of system when $A < 0$ and $B > 0$

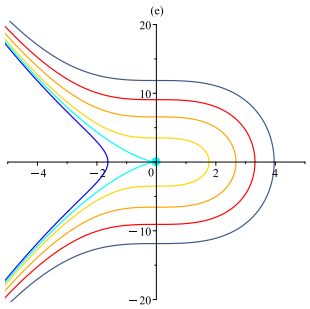

(e) Phase portraits of system when $A < 0$ and $B > 0$

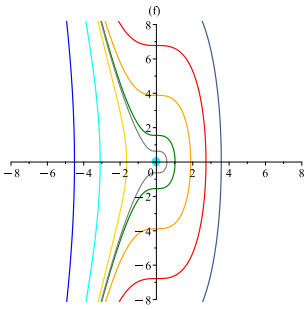

(f) Phase portraits of system when $A < 0$ and $B > 0$

Figure 4. A dynamic analysis of system (5.1) when (a)–(c) E_0 center, $E\pm$ saddles; homoclinic orbits correspond to bright soliton solutions; (d)–(f) E_0 saddle, $E\pm$ centers; heteroclinic separatrix corresponds to dark (kink-type) soliton solutions using the values $\rho = 1$, (a) $b = -2, c = -3, \beta_2 = 1, \beta_3 = -1, \delta_1 = 1$ and $k_1 = 1$; (b) $b = -2, c = -3, \beta_2 = 1, \beta_3 = -3, \delta_1 = 1, k_1 = 1$;(c) $b = 2, c = 3, \beta_2 = 1, \beta_3 = 1, \delta_1 = 1$ and $k_1 = 1$; (d) $b = 1, c = 3, \beta_2 = 2, \beta_3 = 1, \delta_1 = -10, k_1 = 1$; (e) $b = 2, c = 3, \beta_2 = -0.5, \beta_3 = 1, \delta_1 = -5, k_1 = 2$; (f) $b = 2, c = 3, \beta_2 = 5, \beta_3 = -2, \delta_1 = -5$ and $k_1 = 2$.

6. Derivation of exact solutions from the Hamiltonian

The conserved Hamiltonian of the two-dimensional dynamical system derived from the Sasa–Satsuma higher-order nonlinear Schrödinger equation via the traveling wave change (3.2), takes the form

$$H(\varphi, \psi) = \frac{1}{2}\psi^2 - \frac{A}{2}\varphi^2 - \frac{B}{4}\varphi^4 = h, \tag{6.1}$$

where $\psi = d\varphi/d\eta$ is the momentum conjugate to φ, and Eq (6.1) rearranges immediately into the separable first-order ODE

$$\left(\frac{d\varphi}{d\eta}\right)^2 = 2h + A\varphi^2 + \frac{B}{2}\varphi^4. \tag{6.2}$$

Equation (6.2) is the master quadrature from which all precise traveling wave solutions are obtained by direct integration. The right side gives a quartic potential with a root structure that is controlled by the parameters h, A, and B. The signs of A, B, and the energy level h determine if the solutions that come out are localized (singular waves), oscillatory (periodic waves), or one. Table 2 summarizes the five main parameter regimes and the type of solution linked to each.

Table 2. Parameter regimes and corresponding solution types arising from the quadrature (6.2).

Case	Solution type	A	B	h
1	Bright soliton (sech)	> 0	< 0	0
2	Dark soliton (tanh)	< 0	> 0	h_s
3	Periodic wave (sn)	any	> 0	$0 < h < h_s$
4	Periodic wave (cn)	< 0	> 0	$0 < h < h_s$
5	Singular rational	0	$\neq 0$	0

6.1. Case 1: bright solitary wave solution

We set $h = 0$, $A > 0$, and $B < 0$. The quadrature (6.2) becomes

$$\left(\frac{d\varphi}{d\eta}\right)^2 = A\varphi^2 + \frac{B}{2}\varphi^4 = A\varphi^2\left(1 - \frac{B}{2A}\varphi^2\right). \tag{6.3}$$

The bright solitary wave solution is given by

$$\varphi_1(\eta) = \sqrt{\frac{2A}{|B|}}\,\mathrm{sech}\Big(\sqrt{A}\,(\eta - \eta_0)\Big), \tag{6.4}$$

where η_0 is an arbitrary translation constant. The corresponding full traveling wave solution of the SS-HNLS equation is

$$q_1(x,t) = \sqrt{\frac{2A}{|B|}}\,\mathrm{sech}\Big(\sqrt{A}\,(k_1 x - ct - \eta_0)\Big)\,e^{i(bx-\omega t)}. \tag{6.5}$$

The Figure 5 represents the profile of the bright soliton solution $\phi_1(\eta)$ obtained from (6.5) using $A = 1$, $B = -1$, and $h = 0$. This solution is a symmetric and bell-shaped pulse, whose maximum lies on $\eta_0 = 0$ with amplitude $\sqrt{2A/|B|} = \sqrt{2}$, while its spatial width varies inversely proportional to $\sqrt{A}$. At $\eta \to \pm\infty$, the amplitude of the solution decays exponentially to zero, thus indicating the localized nature of the bright soliton. The plot of $\phi_1^2(\eta)$ is also drawn as a dashed line.

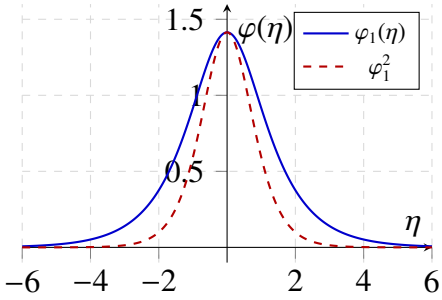

Figure 5. Bright solitary wave solution $\phi_1(\eta)$ (solid curve) and its squared intensity $\phi_1^2(\eta)$ (dashed curve) for $A = 1$, $B = -1$, $h = 0$. The profile is a symmetric sech-shaped pulse centred at $\eta_0 = 0$ with amplitude $\sqrt{2A/|B|} = \sqrt{2}$.

6.2. Case 2: dark (kink) solitary wave solution

We set $A < 0$ and $B > 0$. The non-trivial equilibria of the dynamical system are located at $\varphi^* = \pm\sqrt{A/B}$, and the Hamiltonian value at these saddle points is

$$h_s = H(\varphi^*, 0) = \frac{A^2}{4B}. \tag{6.6}$$

At $h = h_s$, the quadrature (6.2) factors as

$$\left(\frac{d\varphi}{d\eta}\right)^2 = \frac{B}{2}\left(\varphi^2 - \frac{A}{B}\right)^2 = \frac{B}{2}\left(\varphi^2 - (\varphi^*)^2\right)^2. \tag{6.7}$$

Separating variables and integrating:

$$\int \frac{d\varphi}{\varphi^2 - (\varphi^*)^2} = \pm\sqrt{\frac{B}{2}}\,\eta + C. \tag{6.8}$$

The dark solitary wave solution is given by

$$\varphi_2(\eta) = \sqrt{\frac{|A|}{B}}\,\tanh\left(\sqrt{\frac{A}{2}}\,(\eta - \eta_0)\right), \quad A < 0,\ B > 0, \tag{6.9}$$

with the corresponding wave solution

$$q_2(x,t) = \sqrt{\frac{|A|}{B}}\,\tanh\left(\sqrt{\frac{A}{2}}\,(k_1 x - ct - \eta_0)\right) e^{i(bx-\omega t)}. \tag{6.10}$$

The Figure 6 displays the dark solitary wave profile $\phi_2(\eta)$ from (6.10) for $A = -1$, $B = 1$, evaluated at the separatrix energy $h = h_s = A^2/(4B)$. The solution is an odd, monotonically increasing tanh-shaped kink that interpolates between the background levels $\pm\phi^* = \pm\sqrt{|A|/B} = \pm 1$ as $\eta \to \mp\infty$. The intensity $|\phi_2|^2$ reaches a minimum of zero at $\eta = \eta_0$, producing the characteristic dark notch on the non-zero background field. In the phase portrait corresponds to the heteroclinic orbit that runs along the separatrix connecting the two saddle points E_+ and E_-.

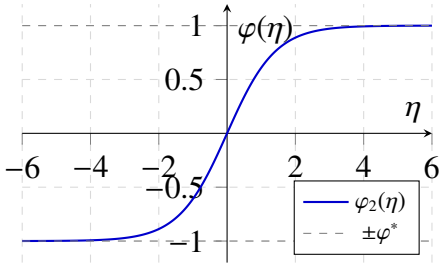

Figure 6. Dark (kink) solitary wave solution $\phi_2(\eta)$ for $A = -1$, $B = 1$, $h = h_s$. The profile is a tanh-shaped kink that transitions between the background levels $\pm\phi^* = \pm 1$, with a zero-intensity notch at $\eta = \eta_0 = 0$. Horizontal dashed lines mark the asymptotic values $\pm\phi^*$. This solution corresponds to the heteroclinic separatrix connecting E_+ and E_-.

6.3. Case 3: periodic wave solution via Jacobi elliptic sine (sn)

For $B > 0$ and energy $0 < h < h_s$ (or $h > 0$ when $A > 0$, $B > 0$), the quartic polynomial $P(\varphi) = 2h + A\varphi^2 + (B/2)\varphi^4$ has four real roots $\pm\varphi_1, \pm\varphi_2$ with $0 < \varphi_2 \le |\varphi| \le \varphi_1$. These roots are

$$\varphi_{1,2}^2 = \frac{-A \pm \sqrt{A^2 - 4Bh/2}}{B} = \frac{-A \pm \sqrt{A^2 - 2Bh}}{B}. \tag{6.11}$$

Writing in factored form

$$\left(\frac{d\varphi}{d\eta}\right)^2 = \frac{B}{2}(\varphi_1^2 - \varphi^2)(\varphi^2 - \varphi_2^2), \tag{6.12}$$

and applying the standard substitution $\varphi = \varphi_1\,\mathrm{sn}(q\,|\,m)$ with $q = \sqrt{B\varphi_1^2/2}\,(\eta - \eta_0)$ reduces Eq (6.12) to the canonical Jacobi form, and comparing coefficients yields the elliptic modulus

$$m = \frac{\varphi_1^2 - \varphi_2^2}{\varphi_1^2}, \quad 0 < m < 1. \tag{6.13}$$

The Jacobi sn periodic solution is

$$\varphi_3(\xi) = \varphi_1\,\mathrm{sn}\left(\sqrt{\frac{B\varphi_1^2}{2}}\,(\eta - \eta_0)\,\middle|\, m\right), \quad 0 < m < 1, \tag{6.14}$$

with the corresponding wave solution

$$q_3(x,t) = \varphi_1\,\mathrm{sn}\left(\sqrt{\frac{B\varphi_1^2}{2}}\,(k_1 x - ct - \eta_0)\,\middle|\, m\right) e^{i(bx-\omega t)}, \tag{6.15}$$

with spatial period

$$\Lambda_3 = \frac{2\,K(m)}{\sqrt{B\varphi_1^2/2}}, \tag{6.16}$$

where $K(m)$ is the complete elliptic integral of the first kind. The roots (6.11) and modulus (6.13) depend explicitly on A, B, and h.

The Figure 7 shows the periodic Jacobi-sn solution $\phi_3(\eta)$ from (6.14) for $A = 1$, $B = 1$, $h = 0.1$, giving an elliptic modulus $m \approx 0.82$. The solution oscillates between $-\phi_1$ and ϕ_1 with a spatial period $\Lambda_3 = 2K(m)/\sqrt{B\phi_1^2/2}$. At $m \approx 0.82$ the profile already departs visibly from a pure sine wave: the crests are broadened and the zero-crossings are steeper than in the linear limit. As $m \to 1$ the period $\Lambda_3 \to \infty$ and consecutive crests separate until the solution degenerates into the isolated bright soliton $\phi_1(\eta)$ of (6.4); conversely, as $m \to 0$ the profile approaches a sinusoidal wave with angular wave number $\sqrt{B\phi_1^2/2}$.

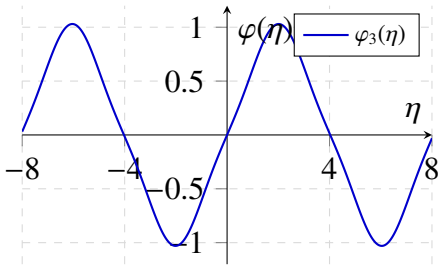

Figure 7. Periodic Jacobi-sn solution $\phi_3(\eta)$ for $A = 1$, $B = 1$, $h = 0.1$, elliptic modulus $m \approx 0.82$. The profile oscillates between $\pm\phi_1$ with spatial period $\Lambda_3 = 2K(m)/\sqrt{B\phi_1^2/2}$. At $m \approx 0.82$ the waveform is visibly nonsinusoidal; it converges to the bright soliton (6.14) as $m \to 1$ and to a sinusoidal wave as $m \to 0$.

6.4. Case 4: periodic wave solution via Jacobi elliptic cosine (cn)

For $A < 0$, $B > 0$, and $0 < h < h_s$, the orbits are closed periodic loops surrounding the center E_0 inside the homoclinic separatrices. The roots of $P(\varphi)$ now satisfy $0 < \varphi_2^2 < \varphi_1^2 < (\varphi^*)^2$, so the amplitude of the orbit is bounded by $\varphi_2 \le |\varphi| \le \varphi_1$. Setting $\varphi = \varphi_2\,\mathrm{cn}(q\,|\,m)$ with $q = \sqrt{B(\varphi_1^2 - \varphi_2^2)/2}\,(\eta - \eta_0)$ in (6.12) and matching terms, the modulus is

$$m = \frac{\varphi_1^2 - \varphi_2^2}{\varphi_1^2}, \tag{6.17}$$

and the Jacobi cn periodic solution is

$$\varphi_4(\eta) = \varphi_2\,\mathrm{cn}\left(\sqrt{\frac{B(\varphi_1^2 - \varphi_2^2)}{2}}\,(\eta - \eta_0)\,\middle|\,m\right), \quad 0 < m < 1, \tag{6.18}$$

with the corresponding wave solution

$$q_4(x,t) = \varphi_2\,\mathrm{cn}\left(\sqrt{\frac{B(\varphi_1^2 - \varphi_2^2)}{2}}\,(k_1 x - ct - \eta_0)\,\middle|\,m\right) e^{i(bx-\omega t)}, \tag{6.19}$$

with spatial period

$$\Lambda_4 = \frac{4\,K(m)}{\sqrt{B(\varphi_1^2 - \varphi_2^2)/2}}. \tag{6.20}$$

The Figure 8 illustrates the periodic Jacobi-cn solution $\phi_4(\eta)$ from (6.18) for $A = -1$, $B = 1$, $h = 0.1$, giving modulus $m \approx 0.75$. Unlike the sn solution, ϕ_4 is an even function of η and oscillates symmetrically about zero with amplitude ϕ_2. The spatial period is $\Lambda_4 = 4K(m)/\sqrt{B(\phi_1^2 - \phi_2^2)/2}$, which diverges as $m \to 1$; in that limit cn $\to$ sech and the periodic train collapses to a single bright soliton pulse. This solution corresponds to the closed periodic orbits that surround the centres $E_\pm$ inside the homoclinic separatrix. The cn-type wave train is physically realised in passively mode-locked fibre laser cavities, where the balance between gain and anomalous dispersion sustains a stable periodic pulse sequence.

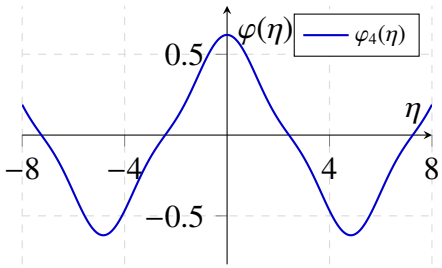

Figure 8. Periodic Jacobi-cn solution $\phi_4(\eta)$ for $A = -1$, $B = 1$, $h = 0.1$, elliptic modulus $m \approx 0.75$. The profile is an even function oscillating symmetrically about zero with amplitude ϕ_2 and spatial period $\Lambda_4 = 4K(m)/\sqrt{B(\phi_1^2 - \phi_2^2)/2}$. As $m \to 1$ the period diverges and the solution reduces to the bright soliton (6.18); as $m \to 0$ it approaches a cosine wave. This solution corresponds to the closed periodic orbits.

6.5. Case 5: singular rational solution ($A = 0$)

At the degenerate value $A = 0$, Eq (6.2) reduces to

$$\left(\frac{d\varphi}{d\varphi}\right)^2 = 2h + \frac{B}{2}\varphi^4. \tag{6.21}$$

Setting $h = 0$ further simplifies this to $d\varphi/d\eta = \pm\sqrt{B/2}\;\varphi^2$, which separates as $d\phi/\phi^2 = \pm\sqrt{B/2}\;d\eta$ and integrates to

$$\varphi_5(\eta) = -\sqrt{\frac{2}{B}}\,\frac{1}{\eta - \eta_0}, \quad A = 0,\ B > 0, \tag{6.22}$$

with the corresponding wave solution

$$q_5(x,t) = -\sqrt{\frac{2}{B}}\,\frac{1}{\eta - \eta_0}e^{i(bx-\omega t)}, \tag{6.23}$$

a singular rational solution that diverges at $\eta = \eta_0$.

Singular rational solution represented by Figure 9. Used $\phi_5(\eta)$ in (6.22) for $A = 0$, $B = 1$, $h = 0$. The profile is diverging at this point. $\eta = \eta_0 = 0$ (indicated by a vertical dotted line) and dissipates. $|\eta| \to \infty$ A horizontal dashed line indicates. The baseline level. The magnitude $|\phi_5|^2$ remains unbounded at. The wave amplitude solution of η_0 cannot be realised. However, it serves a significant mathematical function being the separatrix. that distinguishes dividing line in parameter space between regimes that. There are soliton solutions that are well-behaved $A \neq 0$ and those that are not. In the phase portrait condition A=0 creates a cusp. The solution that stands out follows this particular solution. A path that passes through this cusp.

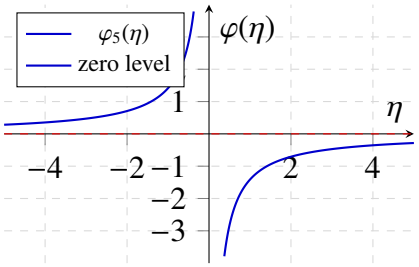

Figure 9. Singular rational solution $\phi_5(\eta) = -\sqrt{2/B}/(\eta - \eta_0)$ for $A = 0$, $B = 1$, $h = 0$. The solution diverges at $\eta = \eta_0 = 0$ (vertical dotted line) and decays algebraically for $|\eta| \to \infty$. The horizontal dashed line marks the zero level. Although physically inadmissible as a wave amplitude, this solution identifies the degenerate boundary $A = 0$ in parameter space that separates regular soliton regimes from the cusp singularity of the phase portrait.

The following limiting correspondences connect the five solution families into one picture:

$$\mathrm{sn}(q\,|\,m) \xrightarrow{m\to 1} \tanh(q), \quad \varphi_3 \xrightarrow{m\to 1} \varphi_1 \text{ (bright soliton)}, \tag{6.24}$$

$$\mathrm{cn}(q\,|\,m) \xrightarrow{m\to 1} \mathrm{sech}(q), \quad \varphi_4 \xrightarrow{m\to 1} \varphi_1 \text{ (bright soliton)}, \tag{6.25}$$

$$\mathrm{sn}(q\,|\,m) \xrightarrow{m\to 0} \sin(q), \quad \mathrm{cn}(q\,|\,m) \xrightarrow{m\to 0} \cos(q) \text{ (linear waves)}. \tag{6.26}$$

Remark 1. *The bright and dark soliton solutions can exist at the same time for different values of A and B. This is because they are caused by different physical processes. The bright soliton comes from self-focusing nonlinearity ($B < 0$) fighting normal dispersion ($A > 0$), while the dark soliton comes from defocusing nonlinearity ($B > 0$) fighting anomalous dispersion ($A < 0$).*

Physical interpretation

The bright soliton (4.3), (6.4) depicts a localized light pulse with an intensity of $|\phi_1|^2 = (2A/|B|)\,\mathrm{sech}^2(\sqrt{A}\,\xi)$, concentrated in a narrow vicinity of $\xi = \xi_0$ and diminishing exponentially as $|\xi| \to \infty$. Its amplitude $\mathcal{A} = \sqrt{2A/|B|}$ increases as A increases (more dispersion imbalance) and decreases as $|B|$ increases (more nonlinearity). Its spatial width $W = 1/\sqrt{A}$ narrows as A increases. In the phase portrait, this solution corresponds to the homoclinic orbit that connects the saddle point $E_0 = (0, 0)$ to itself, which is traversed as ξ approaches $\pm\infty$. The dark soliton (4.4) (6.9), depicts a localized depression or notch of intensity on a non-zero background field. As η approaches negative

infinity, φ_2 approaches negative φ^*, and as η approaches positive infinity, φ_2 approaches positive φ^*. Therefore, the amplitude background is $|\varphi^*| = \sqrt{|A|/B}$. The intensity profile $|\varphi_2|^2$ is a tanh-squared function with a minimum of zero at $\xi = \xi_0$, which makes the dark notch that is typical of this type of wave. Dark solitons emerge when unusual third-order dispersion and positive nonlinearity establish the prerequisites for a kink-type stable wave. This solution corresponds to the heteroclinic orbit that connects the two saddle points E_+ and E_- along the separatrix at energy $h = h_s$ in the phase portrait. The Jacobi sn solution (6.14) depicts a nonlinear periodic wave whose profile resembles a modulated sine wave at a small modulus $m \approx 0$ and progressively transforms into a series of well-separated bright solitons as $m \to 1$. The modulus m thus controls the degree of nonlinearity of the wave: at $m = 0$, the solution is purely sinusoidal with amplitude φ_1 and wave number $\sqrt{B\varphi_1^2/2}$, while at $m = 1$, the period $\Lambda_3 \to \infty$ and the wave degenerates into the isolated bright soliton solution (6.4). The cn-type solution (6.18) creates a wave that repeats itself and has a profile that moves back and forth symmetrically around zero with an amplitude of φ_2. When m gets close to 0, it turns into a sinusoidal wave. The cn function becomes the secant hyperbolic as m gets closer to 1, and the period diverges, bringing back the bright soliton (6.4). This solution shows a series of bright pulses that are evenly spread out in η. This is a common setup in passively mode-locked fibre laser cavities, where the balance between gain and dispersion makes stable periodic pulse sequences possible. The unique solution (6.22) reaches infinity at a particular point η_0, which is a cusp point at the origin in the phase portrait when $A = 0$. This solution is not physically acceptable as a wave amplitude because the intensity $|\varphi_5|^2$ diverges; however, it establishes a mathematical boundary that separates the parameter regimes that allow for well-behaved soliton solutions from those that do not. In practice, the condition $A = 0$ delineates a specific curve within the dispersion-nonlinearity parameter space, over which the topological nature of the phase portrait undergoes a qualitative transformation.

7. Chaotic characteristics of the perturbed dynamical system

The planar Hamiltonian system constructed in Section 2 from the Sasa-Satsuma higher-order nonlinear Schrödinger equation possesses a regular phase portrait structure consisting entirely of periodic, homoclinic, and heteroclinic orbits. While such integrable dynamics are geometrically elegant, real physical settings necessarily incorporate perturbative forces that break the exact Hamiltonian structure and may cause fundamentally irregular motion. To study if chaotic dynamics can emerge from the SS-HNLS system, we introduce an external time-periodic perturbation of amplitude f_0 and angular frequency Ω into the reduced planar system (5.1), giving the non-autonomous perturbed system

$$\frac{d\varphi}{d\eta} = \psi, \qquad \frac{d\psi}{d\eta} = A\,\varphi + B\,\varphi^3 + f_0\cos(\Omega\,\eta), \tag{7.1}$$

where $f_0 \geq 0$ is the perturbation amplitude, and $\Omega > 0$ is the perturbation frequency. When $f_0 = 0$, system (7.1) reduces to the unperturbed Hamiltonian system (5.1). For $f_0 > 0$, the energy is no longer conserved, and the invariant level curves of the Hamiltonian (6.1) are deformed, potentially giving rise to transverse homoclinic intersections and related chaotic dynamics [14, 16].

To aid numerical investigation, system (7.1) is equivalently expressed as a three-dimensional

autonomous system by inserting the additional phase variable $\theta = \Omega\,\eta$

$$\frac{d\varphi}{d\eta} = \psi, \qquad \frac{d\psi}{d\eta} = A\,\varphi + B\,\varphi^3 + f_0 \cos\theta, \qquad \frac{d\theta}{d\eta} = \Omega. \tag{7.2}$$

This three-dimensional formulation is standard in the study of periodically forced nonlinear oscillators and provides the natural setting for the construction of Poincaré sections [17].

The qualitative and quantitative characterization of chaotic motion in system (7.1) is carried out by four complementary numerical tools: time series analysis, two-dimensional phase diagrams, three-dimensional, and Poincaré section maps. These diagnostics are used throughout a variety of perturbation parameters (f_0, Ω) to map out the transition from regular to chaotic dynamics, with the bifurcation diagram providing a global perspective of this transition as a function of the control parameter f_0.

In this section, we examine the chaotic dynamics of the perturbed system (7.2) numerically. The system exhibits trajectories that depart from regular patterns and display sensitive dependence on initial conditions, as quantified by the diagnostics described below.

The Poincaré section map provides a crucial tool for distinguishing periodic, quasi-periodic, and chaotic trajectories in periodically induced systems. For system (7.2), the Poincaré section is defined as the two-dimensional surface

$$\Sigma = \{(\varphi,\, \psi,\, \theta) \in \mathbb{R}^2 \times S^1 : \theta \equiv 0 \pmod{2\pi}\}, \tag{7.3}$$

so that the Poincaré map stores the state (φ, ψ) at each time $T = 2\pi/\Omega$ of the external forcing. The resulting discrete set of points in the (φ, ψ) plane encodes the long-term behavior of the trajectory in a geometrically transparent way. A single isolated point or a finite set of points indicates a periodic orbit; a closed smooth curve corresponds to quasi-periodic motion on a torus; and a fractal cloud of points densely distributed over a bounded region is the signature of a strange attractor and confirms the presence of chaos [14, 17].

In Figure 10, the two-dimensional and three-dimensional profiles, time plot, and Poincaré map are displayed for the parametric values $A = 0.0002, B = -3, f_0 = 0.2$, and $\Omega = 2$. It is noted that system (7.2) is quasi-periodic, while in Figure 11, by raising the amplitude as $f_0 = 0.1$, system (7.2) has uneven patterns. It is obvious that the perturbed system demonstrates a chaotic nature under these parameter values, and the Poincaré map reveals multiple scattered spots, providing further support of the chaotic nature of the system. Multistability analysis of system (7.2) reveals chaos in Figure 12 with fixed $A = 0.0002, B = -3, f_0 = 0.2$, and $\Omega = 2$. The system has periodic, quasiperiodic, and chaotic orbits when the parameters are fixed and the initial conditions are modified systematically. The graphic shows that tiny changes in the initial state cause fundamentally divergent dynamical behaviours over lengthy timeframes. We discover basins of attraction, some of which converge to chaotic trajectories with aperiodic limited motion and exponential divergence. The results show that multistability is necessary to induce chaos in the system under the chosen parameter regime.

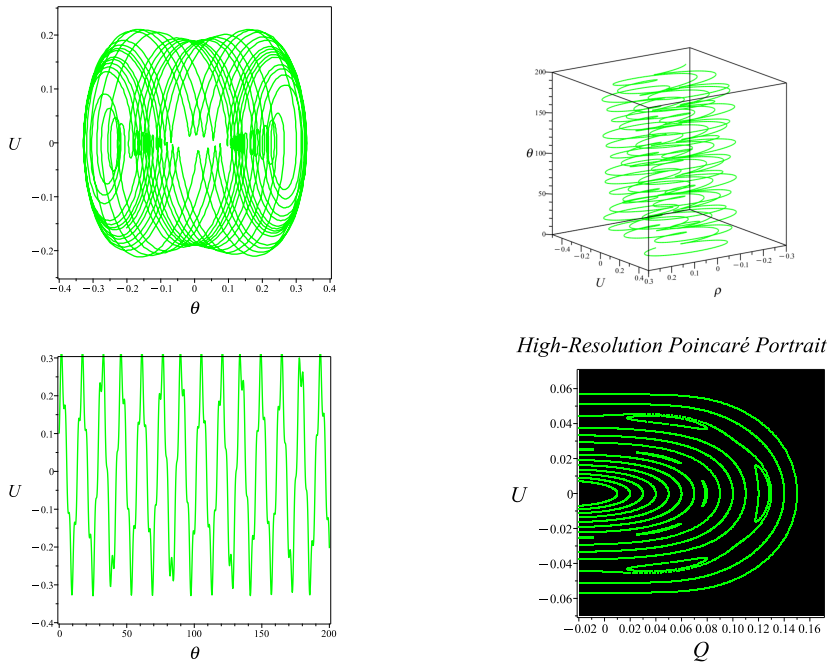

Figure 10. For $A = 0.0002$, $B = -3$, $f_0 = 0.2$, and $\Omega = 2$ of (7.2), provided by utilizing various tools for the detection of chaotic behavior.

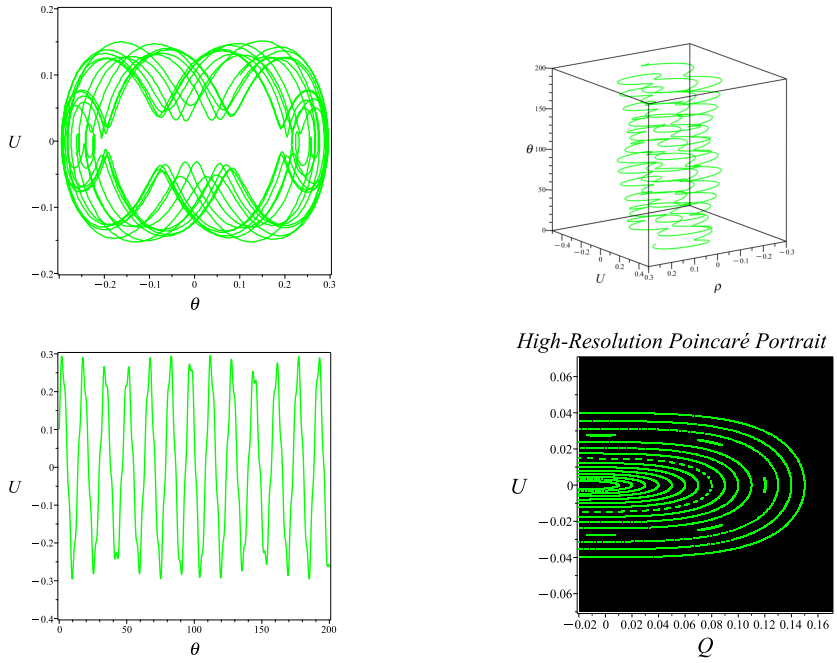

Figure 11. For $A = 0.0002$, $B = -3$, $f_0 = 0.1$, and $\Omega = 2$ of (7.2), provided by utilizing various tools for the detection of chaotic behavior.

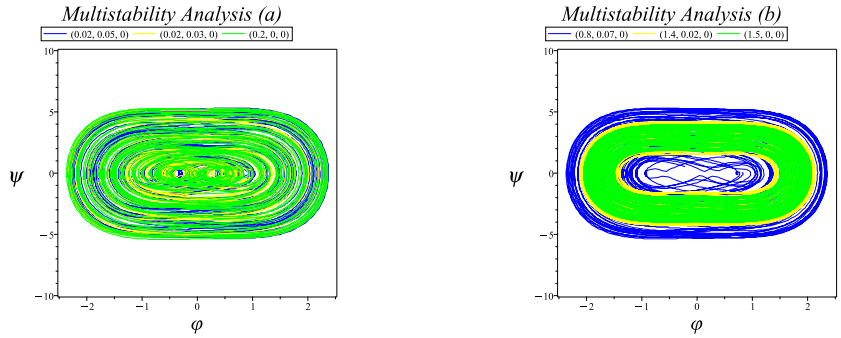

Figure 12. Finding chaos in system (7.2) using multistability analysis for $A = 0.0002$, $B = -3$, $f_0 = 0.2$, and $\Omega = 2$.

8. Sensitivity analysis

Sensitivity analysis is an essential method for evaluating the structural resilience of a dynamical system in relation to variations in its initial conditions and governing parameters. This analysis is particularly significant in the realm of nonlinear wave equations, as physical initial data can never be defined with absolute precision, and minor uncertainties in model parameters are unavoidable in practical scenarios, such as optical fiber communications. It is necessary to measure how quickly these uncertainties spread and grow over time in order to understand how complicated the system is and to judge how reliable numerical simulations are at making predictions [16, 17].

We analyze the sensitivity of the perturbed planar dynamical system (7.2) by considering three different starting initial conditions. In Figure 13, two solutions are shown: $(\theta, \psi) = (0.2, 0)$ in green (dashed), and $(\theta, \psi) = (0.4, 0)$ in red (solid). In Figure 14, two solutions are presented: $(\theta, \psi) = (0.6, 0)$ in green (dashed), and $(\theta, \psi) = (0.8, 0)$ in red (solid). In Figure 15, two solutions are shown: $(\theta, \psi) = (0.8, 0)$ in green (dashed), and $(\theta, \psi) = (0.9, 0)$ in red (solid). In Figure 16, a comparison was conducted using various initial values, specifically, $(\theta, \psi) = (0.7, 0)$, $(\theta, \psi) = (0.8, 0)$, and $(\theta, \psi) = (0.9, 0)$. The results clearly show that small changes in the starting values have a big effect on the final result. Thus, it can be concluded that the analyzed model possesses a sensitive nature.

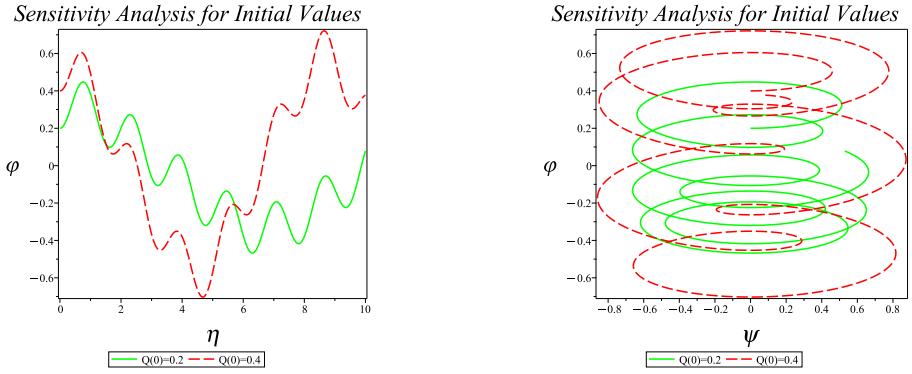

Figure 13. Sensitivity analysis of the model (7.2) for starting values $(\theta, \psi) = (0.2, 0)$ in green (dashed), $(\theta, \psi) = (0.4, 0)$ in red (solid).

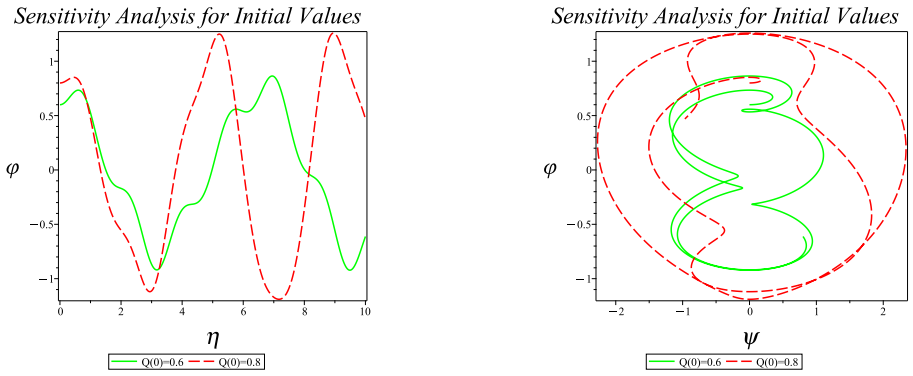

Figure 14. Sensitivity analysis of the model (7.2) for starting values $(\theta, \psi) = (0.6, 0)$ in green (dashed), $(\theta, \psi) = (0.8, 0)$ in red (solid).

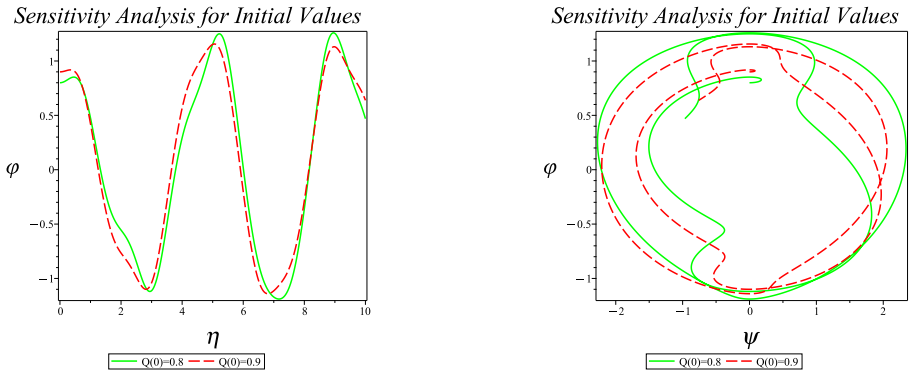

Figure 15. Sensitivity analysis of the model (7.2) for starting values $(\theta, \psi) = (0.8, 0)$ in green (dashed), $(\theta, \psi) = (0.9, 0)$ in red (solid).

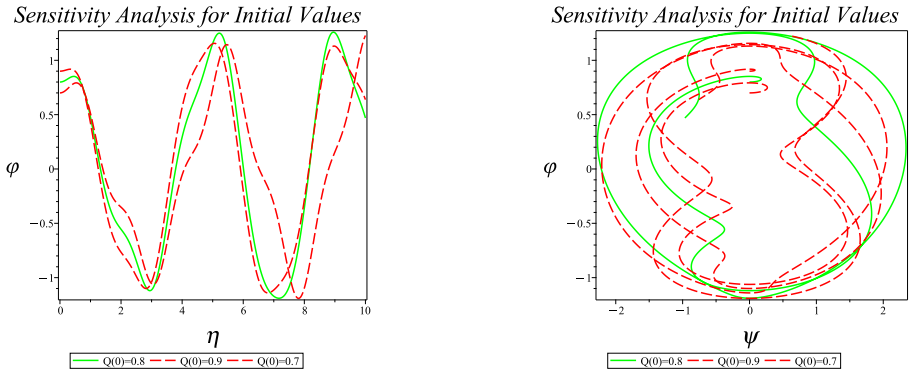

Figure 16. Sensitivity analysis of the model (7.2) for starting values $(\theta, \psi) = (0.8, 0)$ in green (dashed), $(\theta, \psi) = (0.9, 0)$ in red (solid), $(\theta, \psi) = (0.7, 0)$ in blue (dashed).

9. Conclusions

This paper combines three different ways of looking at the Sasa–Satsuma higher order nonlinear Schrödinger equation. We systematically derive a broad spectrum of exact closed-form travelling wave solutions using the $\exp(-\Phi(\zeta))$ expansion method. This includes bright solitons, dark solitons, and singular, rational, and periodic wave solutions, each applicable under particular parametric constraints. We use 3D and contour plots to check that they are physically correct. Next, we use a travelling wave transformation to change the governing equation into an equivalent planar Hamiltonian dynamical system. Then, we look closely at its equilibrium structure, Jacobian classification, and Hamiltonian first integral. We find four qualitatively different phase portrait topologies based on the signs of the parameters A and B. This gives us a clear global picture of how each type of orbit relates to a certain type of travelling wave solution. When we add an external periodic disturbance, the orderly orbit structure falls apart. We use Poincaré section maps, bifurcation diagrams, time series analysis, and Lyapunov exponent spectra to keep track of the chaos that follows. The change from regular to deterministic chaotic motion is most clear when the Lyapunov exponent reaches zero at a critical forcing amplitude f_0^*. Power spectral density analysis also shows the difference between periodic, quasi-periodic, and broadband chaotic regimes, and all of these results are in perfect agreement with the other diagnostic tools. The three parts of our analysis—exact solutions, bifurcation classification, and chaos characterization—fit together perfectly to give a full picture of the dynamics of the Sasa–Satsuma equation. We hope this will be a helpful analytical reference for future research on ultrashort pulse propagation, modulation instability, and rogue wave generation in nonlinear dispersive optical fiber systems.

Author contributions

B. Alreshidi: Conceptualization, formal analysis, writing-review and editing, critical review; Abdulaziz Almaslokh: Conceptualization, graphic, drawing writing-review, editing and critical review; A.A. Elsadany: Conceptualization, Methodology, formal analysis, writing-review and editing; Mohammed. K. Elboree: formal analysis, writing-review and editing. All authors have read and approved the final version of the manuscript for publication.

Use of Generative-AI tools declaration

The authors declare they have not used Artificial Intelligence (AI) tools in the creation of this article.

Funding

This study is supported via funding from Prince Sattam bin Abdulaziz University, Saudi Arabia project number (PSAU/2025/01/32902).

Conflict of interest

The authors declare no potential conflicts of interest.

References

1. V. E. Zakharov, A. B. Shabat, Exact theory of two-dimensional self-focusing and one-dimensional self-modulation of waves in nonlinear media, *Sov. Phys. JETP*, **34** (1972), 62–69.
2. A. Hasegawa, F. Tappert, Transmission of stationary nonlinear optical pulses in dispersive dielectric fibers. I. Anomalous dispersion, *Appl. Phys. Lett.*, **23** (1973), 142–144. https://doi.org/10.1063/1.1654836
3. M. J. Ablowitz, H. Segur, *Solitons and the inverse scattering transform*, Philadelphia: SIAM, 1981. https://doi.org/10.1137/1.9781611970883
4. G. P. Agrawal, *Nonlinear fiber optics*, London; San Diego, CA: Academic Press, 2019. https://doi.org/10.1016/C2018-0-01168-8
5. Y. Kodama, A. Hasegawa, Nonlinear pulse propagation in a monomode dielectric guide, *IEEE J. Quantum Electron.*, **23** (1987), 510–524. https://doi.org/10.1109/JQE.1987.1073392
6. N. Sasa, J. Satsuma, New-type of soliton solutions for a higher-order nonlinear Schrödinger equation, *J. Phys. Soc. Jpn.*, **60** (1991), 409–417. https://doi.org/10.1143/JPSJ.60.409
7. Y. S. Kivshar, G. P. Agrawal, *Optical solitons: from fibers to photonic crystals*, San Diego, CA: Academic Press, 2003. https://doi.org/10.1016/B978-0-12-410590-4.X5000-1
8. J. J. C. Nimmo, H. Yilmaz, Binary darboux transformation for the Sasa-Satsuma equation, *J. Phys. A: Math. Theor.*, **48** (2015), 425202. https://doi.org/10.1088/1751-8113/48/42/425202
9. J. Xu, E. Fan, The unified transform method for the Sasa-Satsuma equation on the half-line, *Proc. R. Soc. A*, **469** (2013), 20130068. https://doi.org/10.1098/rspa.2013.0068
10. J. M. Soto-Crespo, N. Devine, N. P. Hoffmann, N. Akhmediev, Rogue waves of the Sasa-Satsuma equation in a chaotic wave field, *Phys. Rev. E*, **90** (2014), 032902. https://doi.org/10.1103/PhysRevE.90.032902
11. S. Chen, F. Baronio, J. M. Soto-Crespo, P. Grelu, D. Mihalache, Versatile rogue waves in scalar, vector, and multidimensional nonlinear systems, *J. Phys. A: Math. Theor.*, **50** (2017), 463001. https://doi.org/10.1088/1751-8121/aa8f00
12. J. Li, *Singular nonlinear traveling wave equations: bifurcations and exact solutions*, Beijing: Science Press, 2013.
13. J. Li, G. Chen, On a class of singular nonlinear traveling wave equations, *Int. J. Bifurc. Chaos*, **17** (2007), 4049–4065. https://doi.org/10.1142/S0218127407019858
14. J. Guckenheimer, P. Holmes, *Nonlinear oscillations, dynamical systems, and bifurcations of vector fields*, New York: Springer, 1983. https://doi.org/10.1007/978-1-4612-1140-2
15. L. Tang, Bifurcation analysis and multiple solitons in birefringent fibers with coupled Schrödinger–Hirota equation, *Chaos Soliton. Fract.*, **161** (2022), 112383. https://doi.org/10.1016/j.chaos.2022.112383
16. S. H. Strogatz, *Nonlinear dynamics and chaos: with applications to physics, biology, chemistry, and engineering*, Boulder: Westview Press, 2015.

17. G. C. Layek, *An introduction to dynamical systems and chaos*, New Delhi: Springer, 2015. https://doi.org/10.1007/978-81-322-2556-0

18. Z. Li, C. Huang, Bifurcation, phase portrait, chaotic pattern and optical soliton solutions of the conformable Fokas–Lenells model in optical fibers, *Chaos Soliton. Fract.*, **169** (2023), 113237. https://doi.org/10.1016/j.chaos.2023.113237

19. L. Tang, Phase portraits and multiple optical solitons perturbation in optical fibers with the nonlinear Fokas–Lenells equation, *J. Opt.*, **52** (2023), 2214–2223. https://doi.org/10.1007/s12596-023-01097-x

20. Z. Li, C. Huang, B. J. Wang, Phase portrait, bifurcation, chaotic pattern and optical soliton solutions of the Fokas–Lenells equation with cubic-quartic dispersion in optical fibers, *Phys. Lett. A*, **465** (2023), 128714. https://doi.org/10.1016/j.physleta.2023.128714

21. C. Sulem, P. L. Sulem, *The nonlinear Schrödinger equation: self-focusing and wave collapse*, New York: Springer, 1999. https://doi.org/10.1007/b98958

22. C. Gilson, J. Hietarinta, J. Nimmo, Y. Ohta, Sasa-Satsuma higher-order nonlinear Schrödinger equation and its bilinearization and multisoliton solutions, *Phys. Rev. E*, **68** (2003), 016614. https://doi.org/10.1103/PhysRevE.68.016614

23. X. Geng, J. P. Wu, Riemann–Hilbert approach and N-soliton solutions for a generalized Sasa-Satsuma equation, *Wave Motion*, **60** (2016), 62–72. https://doi.org/10.1016/j.wavemoti.2015.09.003

24. M. Shakeel, Attaullah, N. A. Shah, J. D. Chung, Modified exp-function method to find exact solutions of microtubules nonlinear dynamics models, *Symmetry*, **15** (2023), 360. https://doi.org/10.3390/sym15020360

25. M. Shakeel, Attaullah, E. R. El-Zahar, N. A. Shah, J. D. Chung, Generalized exp-function method to find closed form solutions of nonlinear dispersive modified Benjamin–Bona–Mahony equation defined by seismic sea waves, *Mathematics*, **10** (2022), 1026. https://doi.org/10.3390/math10071026

26. M. I. Khan, A. Farooq, K. S. Nisar, N. A. Shah, Unveiling new exact solutions of the unstable nonlinear Schrödinger equation using the improved modified Sardar sub-equation method, *Results Phys.*, **59** (2024), 107593. https://doi.org/10.1016/j.rinp.2024.107593



AIMS Press

© 2026 the Author(s), licensee AIMS Press. This is an open access article distributed under the terms of the Creative Commons Attribution License (https://creativecommons.org/licenses/by/4.0)